Research article

Crack-free in situ heat-treated high-alloy tool steel processed via laser powder bed fusion: microstructure and mechanical properties

Simon Bergmueller [a],[*], Lukas Kaserer [a], Lorenz Fuchs [a], Jakob Braun [a], Nikolaus Weinberger [b], Ilse Letofsky-Papst [c], Gerhard Leichtfried [a]

[a] Faculty of Engineering Sciences, University of Innsbruck, Department of Mechatronics, Materials Science, Technikerstraße 13, 6020 Innsbruck, Austria
[b] Faculty of Engineering Sciences, University of Innsbruck, Department of Structural Engineering and Material Sciences, Material Technology, Technikerstrasse 13, 6020 Innsbruck, Austria
[c] Institute of Electron Microscopy and Nanoanalysis and Center for Electron Microscopy, Graz University of Technology, Steyrergasse 17, 8010 Graz, Austria

G R A P H I C A L   A B S T R A C T
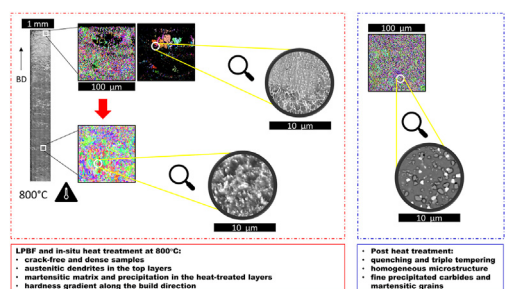
A B S T R A C T

In this study, high-alloy tool steel S390 was processed crack-free and dense for the first time using laser powder bed fusion (LPBF). The resulting mechanical properties and microstructure of the LPBF steel parts were investigated. High-alloy tool steels, such as high-performance high-speed Boehler S390 steel (containing 1.64 wt% C and W, Mo, V, Co, and Cr in the ratio 10:2:5:8:5 wt%), are prone to cracking when processed using LPBF because these steels have high carbon and carbide-forming alloying elements content. Cracks are induced by thermal stresses and solid-phase transformation, combined with weak grain boundaries caused by segregated primary carbides. Substrate plate heating reduces thermal stresses and enables in situ heat treatment, thus modulating solid-phase transformation and carbide precipitation and preventing cracking during cooling. The resulting microstructure, precipitations, and mechanical properties of the as-built LPBF specimens, which were in situ heat-treated at 800 °C, and the conventionally post-heat-treated specimens were assessed using optical microscopy, scanning electron microscopy, transmission electron microscopy, energy-dispersive X-ray spectroscopy, electron backscatter diffraction, X-ray diffraction, hardness testing, bending testing, and density measurement. In situ heat treatment impacts microstructure, precipitation behavior, and solid-phase transformation, causing a change in the microstructure of the material along the build direction due to different thermal histories. The as-built specimens exhibit a hardness gradient along the build direction of 500 HV1 to 800 HV1 in the top layer. The average bending

---

* Corresponding author.
  E-mail address: Simon.Bergmueller@uibk.ac.at (S. Bergmueller).

strength is 2500 MPa, measured from the tensile stresses on the harder side and the compressive stresses on the softer side. Conventional post-heat treatment yields a mean hardness of 610 HV1 and a mean bending strength of 2800 MPa.

1. Introduction

Tools for the aerospace, automotive, and medical technology industries have high requirements for strength, hardness, toughness, temperature, and wear resistance. High-speed steels (HSS) such as the Boehler S390 *Microclean* meet these requirements, exhibit good hot hardness, bending strength, and machinability, and are frequently used to produce milling cutters and drills. Tools made of S390 are currently produced conventionally via powder metallurgy (PM). The established conventional PM manufacturing process is complex and typically involves powder production, hot isostatic pressing (HIP), forging, and subsequent heat treatment with quenching and triple tempering [1, 2, 3, 4, 5]. With additive manufacturing (AM), near-net-shaped tool parts can be fabricated directly from powder raw material without time-consuming or costly intermediate steps. Furthermore, new functions and geometries can be implemented, such as internal cooling channels that extend the lifetime of tools or tool components and/or improve performance. The two most prominent powder bed-based AM processes for tools are electron beam melting (EBM) and laser powder bed fusion (LPBF). High-alloy tool steels such as the S390 (containing 1.64 wt% C and W, Mo, V, Co, and Cr in the ratio 10:2:5:8:5 wt%) are considered non-weldable and prone to cracking. To process HSS using LPBF, adjustments must be made and framework conditions considered. To reduce the thermal gradient and thus avoid crack formation induced by thermal stresses, substrate plate heating is applied during the LPBF fabrication of various materials. Several studies have been performed using substrate plate temperatures of 200–400 °C on HSS steels with relatively low carbon content, e.g., HSS M2 [6, 7, 8] and the HSS M50 [9], all yielding similar defect patterns, i.e., cold cracks. Furthermore, substrate plate heating has been demonstrated to reduce crack density, defect frequency [10, 11], and residual stresses in H13 hot work tool steel [12]. Only a few tool steels can be successfully processed using LPBF without defects [13, 14], not least because of the cold cracking problem [15]. Feuerhahn et al. [16] and Geenen et al. [17] have processed high carbon steel via LPBF with substrate plate heating. Geenen et al. were the first to produce and investigate an HSS (i.e., HSS 1.3344), with a C content of 1.2 wt%, using LBPF at 300 °C [17]. Using LPBF at 350 °C, Saewe et al. managed to process an HSS composed of W, Mo, V, and Co (6:5:3:8 wt%), which already has a high content of carbide formers and carbon (1.2 wt%), without cracking [18] and investigated the influence of the increased C content on this alloy [19]. A recent study by Galbusera et al. investigates the processability and cracking behavior of similar high-alloy tool steels fabricated using LPBF, exploring various analytical and empirical models (e.g., cooling rate, the carbon equivalent, martensite start temperature, solidification interval, and energy density) for shortening the experimental effort invested in alloy design [20]. They conclude that conventional LPBF machines may be inadequate for mitigating the characteristic defects.

Boehler S390 steel is an outstanding model among HSS tool steels characterized by high bending strength (up to 4500 MPa), hardness (up to 68 HRC) [1], temperature resistance, and abrasion resistance, with potential for subsequent machining and heat treatment, whether produced conventionally or via AM. Consequently, it is popular in the industry and has been studied extensively. Over the years, several research projects have been devoted to the study of the S390 PM material [2, 3, 4, 21, 22, 23, 24, 25]. In 2004, Niederkofler et al. were the first to investigate the matrix of this PM-processed tool steel and found 20 nm-sized carbides using the atom probe analysis method [25]. This was followed by extensive characterization of the typical carbides (i.e., MC and M_6C) and the martensite matrix microstructure by Godec et al. in 2010 [4]. The influence of posttreatment, including cryogenic treatment and plasma nitriding, on mechanical properties such as hardness, fracture toughness, and tribology has also been investigated [3, 21]. A recent study investigates heat treatment—specifically, the variation of duration and temperature—and its effect on the mechanical properties, composition, solubility, and precipitation of carbides [2, 23]. These studies confirm that the mechanical properties resulting from heat treatment are advantageous and recommend a heat treatment process that includes quenching and triple tempering for the formation of a martensite matrix and to precipitate micron-sized carbides.

One study examines the AM of S390 using EBM at 780 °C to produce crack-free specimens, extensively characterizes the solidification structure, and investigates the microstructure, carbide precipitation behavior, and mechanical properties [26]. According to this study, dendritic austenitic grains have a size of approximately 50 μm and are the first set of grains to solidify, followed by MC carbides of V and W, which solidify in the interdendritic regions. The morphology of the matrix phase was characterized as a combination of equiaxed dendritic grains and columnar dendritic grains interspersed with primary carbides several micrometers in size, with a primary carbide network of M_2C comprising W, Fe, Mo, and Co in order of significance. At a density of 97.7%, mechanical properties similar to those of conventional PM S390 were obtained with a hardness of 65.5 HRC and a tensile strength of 2600 MPa.

The mechanical properties of steel are influenced by the size of the grains and carbides. Based on the Hall–Petch and Orowan mechanisms, the smaller the grain size, the higher the expected strength, and the smaller the distances of precipitates, the greater the expected hardness, respectively [27, 28]. Dissolved carbide-forming elements can be precipitated as secondary carbides during triple tempering in the form of MC (mainly vanadium carbide), M_6C (mainly Fe_3W_3C) carbides, and the metastable M_2C (containing V, W, Mo, Fe) in the submicrometer range. In addition, triple tempering in the subsequent heat treatment contributes to the transformation of retained austenite (RA) into martensite, with face-centered cubic (FCC) RA transforming into a body-centered (BC) Fe phase—more precisely, into body-centered tetragonal (BCT) martensite, as reported by Peng et al. for this high alloyed steel [23]. The distinction between solidification structures dendrites, cells, and grains should be mentioned here. For AISI 316L (DIN 1.4404), maraging steel (DIN 1.2709), and other materials in LPBF, cellular solidification structures with cell sizes of approx. 500 nm transverse to the extent of the cells and a local misorientation of <2° with respect to each other are reported within grains with high-angle grain boundaries [29, 30, 31]. For HSS in LPBF, a bimodal microstructure with coarse columnar grains (up to 50 μm) and fine equiaxed grains (of approx. 1 μm) exhibiting a dendritic substructure is reported [19].

This study is the first to investigate the microstructure and mechanical properties of HSS S390 specimens produced via LPBF. HSS S390 specimens produced under as-built and heat-treated conditions are compared against conventionally produced PM HSS and EBM HSS.

2. Materials and methods

2.1. Powder characterization

The material used is the as-atomized powder of PM Boehler S390 Microclean steel. The chemical composition of the powder was determined by the manufacturer by combustion analysis (C, S), carrier gas hot extraction (O), and inductively coupled plasma optical emission spectrometry (remaining elements). The results are listed in Table 1. The atomized S390 powder was sieved through a 63-μm sieve, resulting in particle size distributions (PSD) of D_{10} 15 μm, D_{50} 37 μm, and D_{90} 66 μm

determined with the Mastersizer 3000 (Malvern Instruments, UK). The sieved powder was then vacuum-dried. The solid density of this material is 8.1 g/cm^3, according to Boehler Edelstahl [1]. The bulk density, tap density, and flowability of the powder were determined to be 4.57 g/cm^3, 5.21 g/cm^3 and 18.77 g/s, respectively. Figure 2 presents a scanning electron microscope (SEM) image of the predominantly spherical powder.

2.2. LPBF production and heat treatment

A customized Aconity3D LPBF system (Aconity3D GmbH, Germany) equipped with a 400 W IPG Nd-YAG laser (IPG Laser GmbH, Germany) and a substrate plate that can be heated to a temperature of 800 °C was used for the production of specimens. Argon was used as a process gas, and the oxygen level in the building chamber was kept below 20 ppmv. A nominal layer thickness of 30 μm was used for all the experiments, and for each layer, the hatch pattern was rotated by 67°. Hatch spacing was varied from 60 to 120 μm. Stripe and island scan strategies were used, with scan vectors in meander sequence (zigzag), and the vector lengths were varied from 2.5 to 10 mm. At least four specimens were prepared for density measurement and bending tests. All the specimens were separated from the substrate plate using wire electrical discharge machining (EDM). For the preliminary parameter study, single walls and cubes were produced to limit the parameter window. To quantify the energy input, the volumetric energy density E$_V$ was used, given by Eq. (1):

$$E_v = \frac{P_L}{v_s \cdot t \cdot h_d} \left[\frac{J}{mm^3} \right] \tag{1}$$

where P$_L$ is the laser power, v$_s$ is the laser scan speed, t is the nominal layer thickness, and h$_d$ is the hatch distance. P$_L$ and v$_s$ were varied through a wide range to optimize the specimens in terms of density and cracks. The optimized process parameters are presented in Table 2.

Before running the LPBF build job, the substrate plate was heated up continuously for 2 h to a building temperature of 800 °C. The actual building time starts at the application of the first powder layer and the subsequent fusion of the first layer. With the height of the cubic specimens of 10 mm, the build time on this LPBF system (i.e., until the last layer is fused) is about 3 h. The LPBF process is followed by controlled cooling of the specimens for 180 min in the powder bed to, as much as possible, prevent cracking during cooling. Of the as-built specimens, half were subsequently heat-treated, and hereafter referred to as heat-treated (HT) specimens. The heat treatment consisted of austenitizing at 1150 °C, quenching in oil for 4 min, tempering three times at 570 °C for 2 h each, and cooling in air. The heat treatment was conducted in a Nabertherm muffle furnace (L/9/12/P320, Nabertherm, Germany).

2.3. Microstructural characterization

The embedded specimens were ground with abrasive papers with a grit size of 80–2,400 following standard procedures and then polished with 3 μm and 1 μm diamond suspensions (Struers, Germany). The light optical microscope examination was conducted at ×100 magnification using an Alicona InfiniteFocus G4 (Alicona Imaging GmbH, Austria) at the polished specimens etched with nital (4% alcoholic nitric acid). SEM examinations were performed using an FEI Quanta 200F field emission gun scanning electron microscope and a JSM-7610F scanning electron microscope (Jeol, Japan), which is additionally equipped with an energy-dispersive X-ray spectroscopy (EDX) system (EDAX, USA), using an acceleration voltage of 15 kV. Although the determination of the

quantitative content leads to a high relative error for certain elements (such as carbon), especially at low concentrations, the measurement was nevertheless performed for all listed alloying elements, and the relative error was listed in order to be able to discuss the results systematically. Transmission electron microscopy (TEM) examinations were conducted using an FEI Tecnai F20 microscope equipped with a Schottky field emission gun at an accelerating voltage of 200 kV. EDX spectra were acquired with an EDAX Si(Li) detector, and elemental maps were obtained using a GATAN imaging filter and an Ultra-Scan CCD camera. Electron backscatter diffraction (EBSD) measurements were performed using a Zeiss Ultra 55 Plus with a forward scatter detector (FSD), using an acceleration voltage of 20 kV. A step size of 0.25 μm was used for the 250 μm sections, and 0.05 μm for the 50 μm sections. TEM and EBSD investigations and the respective specimen preparation were conducted at the Austrian Centre for Electron Microscopy and Nanoanalysis (FELMI-ZFE) in Graz. Phase analysis of the powder, the as-built specimens, and heat-treated specimens were performed via X-ray diffraction (XRD) using an Empyrean Panalytical diffractometer (Malvern Panalytical Ltd., UK) in a Bragg–Brentano configuration, with Cu Kα radiation between 15° and 110°. The relative density of all cube-shaped specimens (10 × 10 × 10 mm) was measured using Archimedes' principle, and also further confirmed for some specimens using metallographic density determination.

2.4. Mechanical testing

The three-point bending test was performed at ambient temperature in line with the DIN EN ISO 7438:2020 standard on polished as-built specimens (5 × 5 × 35 mm) on a Shimadzu AGS-10kNX (Shimadzu, Japan) universal testing machine. The testing force was applied in the direction opposite to the build direction, and the test was performed four times for each parameter configuration. The Vickers hardness test (HV1) was performed in compliance with the DIN ISO 6507 standard using the Shimadzu HMV-*G microhardness* tester device (Shimadzu, Japan). When measuring the hardness gradient across the building height, three hardness values were averaged in each case.

3. Results

3.1. Powder properties

The as-atomized S390 PM powder has a wide size distribution, with larger particles than the powder typically used in LPBF. Sieving with a mesh size of 63 μm separated the unwanted large particles, thus establishing a PSD suitable for LPBF. Figure 1 shows the size PSD of the powder before and after sieving, measured using laser diffraction. Table 3 lists the associated characteristic diameters D$_{10}$, D$_{50}$, and D$_{90}$, and the bulk density, tap density, Hausner ratio, and flowability. Both the bulk density and the tap density were reduced by sieving the coarse fractions. The Hausner ratio did not change. However, compared to the as-delivered condition, the flowability of the powder improves significantly after sieving. Figure 2 shows SEM images of the sieved powder. The majority of particles possess spherical morphology; however, there is a small fraction of deformed particles and particles with satellites (Figure 2(a)). In the powder cross section presented in Figure 2(b) and Figure 2(d), only a few small pores with diameters of <10 μm are visible. A high-resolution image of a powder particle surface taken in secondary-electron (SE) mode (Figure 2(c)) indicates that the grains grew dendritically during solidification. A high-resolution image of a polished cross section taken in backscattered electron (BSE) mode (Figure 2)

Table 1. Chemical composition of PM HSS S390 Microclean according to the supplier, voestalpine Boehler Edelstahl GmbH & Co KG, Austria.

Elements	Fe	C	W	Mo	V	Co	Cr	Ni	Mn	Si	S	P	O
wt%	bal.	1.64	10.09	2.28	5.12	8.32	4.91	0.20	0.26	0.30	0.018	0.018	0.0041

Table 2. Optimized process parameters determined experimentally in a preliminary parameter study.

	Laser power, P_L (W)	Scan velocity, v_s (mm/s)	Hatch distance, h_d (μm)	Nominal layer thickness, t (μm)	Volumetric energy density, E_V (J/mm³)	Scan strategy	Scan vector length (mm)	Substrate plate temperature (°C)
Preliminary study	100–400	400–2000	60–120	30	16.7–333.3	Lines/ Islands/ Stripes	2.5–10	500, 600, 800
Optimized parameter	130	800	100	30	54.2	Stripes	5	800
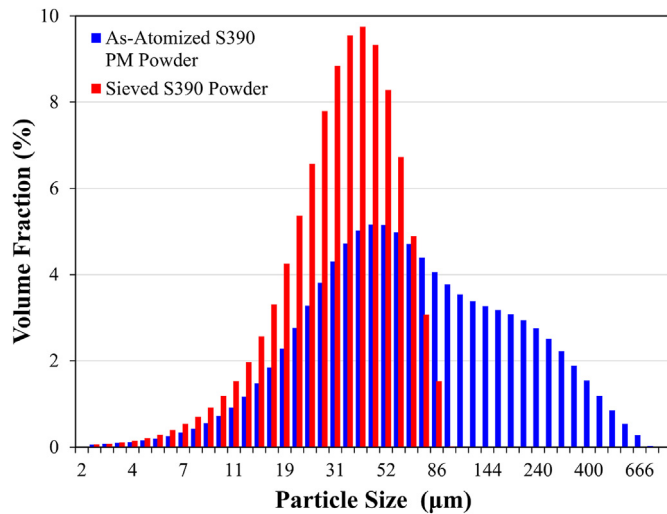
Figure 1. PSD measured using laser diffraction: particle size and distribution (volume fraction) of the as-atomized PM Boehler S390 powder and the sieved powder used in LPBF.

reveals austenitic dendrites as the primary solidification structure, with segregated primary carbides in the interdendritic regions or at the grain boundaries.

3.2. Microstructure

Figure 3(a) shows a light optical microscopy (LOM) image of the cross section of a cubic specimen across the building height of the specimen. The brightness of the etched areas changes along the buildup direction. The difference between the top and bottom regions is confirmed in the detailed crystal orientation maps derived via EBSD in inverse pole figure (IPF) coloring. In Figure 3(b), the IPF mapping of the FCC phase of the top region [upper red square in Figure 3(a)] of the specimen shows coarse columnar grains. From Figure 3(c), it can be seen that the microstructure of the top region of the specimen consists predominantly of fine BC phase without a pronounced texture. The FCC phase fractions and pores appear black in this IPF mapping. In the center area (Figure 3(d)) the FCC phase appears as finely distributed dots in this magnification. The same applies for the bottom area as revealed in Figure 3(f). Large columnar FCC grains cannot be detected in the center or in the bottom area. The grain structure of the BC phase in the center (Figure 3(e)) and the bottom area of the specimen (Figure 3(g) does not show a pronounced texture.

Figure 4 shows SEM micrographs of a 50 × 50 μm section of the center region of the as-built specimens. Figure 4(a) presents an IQ (image quality) image in which lighter areas and darker areas (which indicate a low-quality electron backscattering pattern) can be distinguished. In Figure 4 (b), the FCC phase fraction that can be resolved at this magnification and step size is shown in IPF coloring. The regions marked in Figure 4(a) are also marked in Figure 4(b). It can be seen that the FFC phase components that can be resolved at this magnification have the same crystal orientation within each marked region. Figure 4(c) shows the IPF mapping of the BC phase fraction; again, no preferential orientation of the BC phases is evident. Furthermore, the darker areas marked in Figure 4(a) are also marked in yellow in Figure 4(c). In Figure 4 (d) the etched surface of the center area of the as-built specimen is shown as an overlay of the SE and BSE detector. The semicircular red dashed lines indicate meltpool borders from which radially directed columnar structures originate (black arrows), transitioning to a fine globular structure (indicated in blue).

Figure 5(a) is an SEM BSE image of the center region of an as-built specimen with columnar dendritic grains. Precipitated segregations are bright in BSE mode, indicating elements with high atomic mass (atomic number). Figure 5(b) is an SEM image in BSE mode of the center region of the heat-treated specimen, in which precipitates embedded in a martensitic matrix are visible.

Figure 6 shows TEM high-angle annular dark-field (HAADF) images of a dendritic area at the center of an as-built specimen with cellularly arranged interdentritic segregations. Elemental mappings show that Co is predominant in the Fe matrix, while the interdentritic segregations are depleted of Fe and Co. Cr and C are also dissolved in the Fe matrix. The segregations can be identified as carbides, composed predominantly of V, W, Mo, Cr, and C. In the upper part of the Cr mapping, a carbide with high Cr content is visible, with W next to it, but little V. Furthermore, S impurities are found in the segregations and in the Fe matrix.

Figure 7 shows SEM EBSD micrographs of a 250 × 250 μm (7(a)) and a 50 × 50 μm (7(b)) section of the heat-treated specimen. At the higher magnification (7(b)), homogeneously distributed black areas can be seen corresponding to the unindexed FCC or other non BC phases.

Figure 8 presents SEM BSE micrographs of the heat-treated specimens. In Figure 8(a), it can be seen that the carbides are evenly distributed. Figure 8 (b) shows the precipitated carbides distinguished in the BSE in white and gray. Figure 8 (c) shows, in detail, a cluster with different phases embedded in the matrix. Figure 8(d) shows an EDX mapping of the cluster in Figure 8(c), followed by mappings of individual elements. The white phases in the BSE plot are rich in W, Fe, and C, while the gray phases are rich in V and C and some Cr. The black phase in Figure 8(c) is rich in S, Fe, and Co, and the surrounding matrix consists of Fe with Co, Cr, and C dissolved in it.

Figure 9 shows the BSE SEM micrograph of the section of Figure 8 with four different phases identified via EDX, with the wt% indicated. The matrix is highlighted in yellow. Co (12 wt%) and Cr (5 wt%) are the predominant elements dissolved in the martensitic Fe matrix with about 1 wt% C. The proportions of carbide-forming elements V, W, and Mo are low. W and Fe are the predominant elements detected in the area marked

Table 3. Powder characterization with laser diffraction and bulk density, tap density, and flowability measurements.

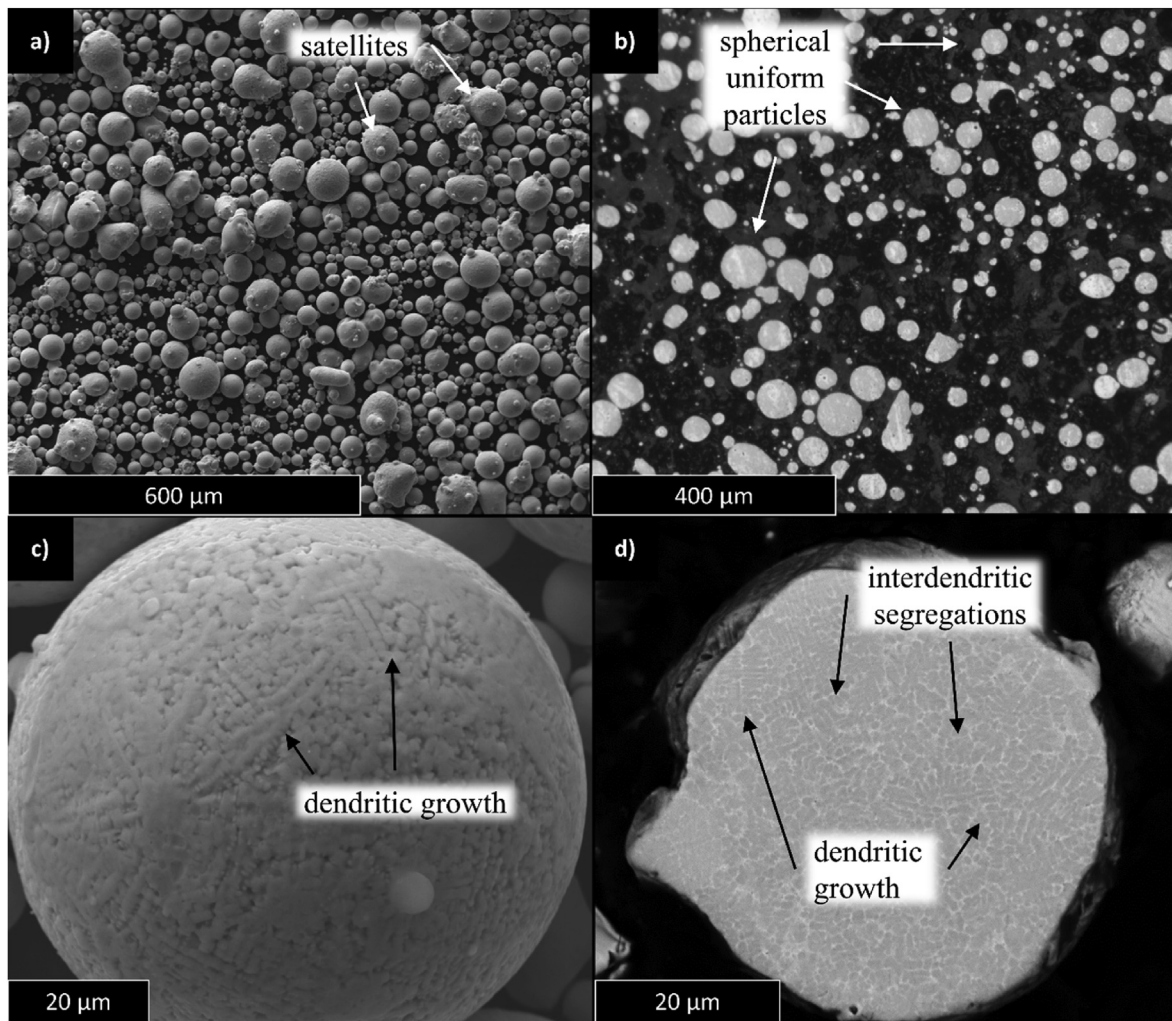| Material	D_{10} (μm)	D_{50} (μm)	D_{90} (μm)	Bulk Density (g/cm³)	Tap Density (g/cm³)	Hausner ratio	Flowability (g/s)
As-atomized PM S390 Powder	20.6 ± 0.2	69.7 ± 2.7	292 ± 14.4	5.06 ± 0.08	5.97 ± 0.08	1.18	12.02 ± 1.10
Sieved S390 Powder	15.5 ± 0.3	36.7 ± 0.1	66.3 ± 0.2	4.57 ± 0.02	5.21 ± 0.06	1.14	18.77 ± 6.45

Figure 2. SEM images of the sieved S390 powder: (a) shows powder particles with few satellites in SE mode; (b) a powder cross section shows dominantly spherical uniform-shaped particles without inner porosity; (c) detailed view of a spherical particle in SE mode, with dendritic growth on the particle surface; (d) dendritic growth and interdendritic segregations visible in the cross section of a particle in BSE mode.

with a red square (38 wt% and 35 wt%, respectively), with elevated levels of the other carbide-forming elements and carbon. The green square marks the phase, which is dominated by V (38 wt%) and has a high Cr and C content (7 wt% and 6 wt% respectively). W, Fe, and Mo are also present in the area. The black phase is marked in blue as an impurity and shows a segregation of Mn (14 wt%) associated with S (10 wt%) and Fe.

Phase analysis of the powder for LPBF, the as-built parts in the top layers and bottom layers, and the heat-treated specimens is presented in Figure 10. The XRD patterns of the specimens show characteristic peaks for the dominant Fe phases: austenite FCC, martensite BCT, and ferrite BCC, and the carbides MC and M_6C are also identifiable. For the powder, peaks of austenite and MC are visible. For the as-built top layer, austenite peaks, martensite double peaks, and MC are visible. In the as-built bottom layer, BCT patterns are visible, in addition to a weak MC peak. In the heat-treated condition, prominent peaks are observed for BCT and M_6C, accompanied by a slight MC peak.

3.3. Mechanical properties

The results of the bending tests are plotted in Figure 11, which shows that the strength of the specimens increases after heat treatment. The gradient of hardness along the height of the specimen is presented in Figure 12. For the as-built specimens, a gradient of hardness is observed,

with the increasing height measured in mm increments and the last built top layers having the highest hardness values. The heat-treated specimens show no hardness trend. Table 3 presents two mechanical properties: bending strength and Vickers hardness (HV1) of the as-built and heat-treated specimens. The mean values, including the maximum and minimum of both the bending strength and hardness, are also presented in Table 3. The as-built specimens exhibit a mean bending strength of 2535 MPa, with a maximum value of 2775 MPa and a minimum of 2330 MPa. The hardness of the as-built specimens ranges from 499 HV1 in the lower layers to 798 HV1 in the top layer. The heat-treated specimens exhibit a mean bending strength of 2799 MPa, with a maximum value of 3504 MPa and minimum of 2613 MPa. The mean hardness of the heat-treated specimens is 611 HV1, with a 663 HV1 maximum and 561 HV1 minimum, without a trend along the height of the specimen.

4. Discussion

The Boehler S390 Microclean powder used for the tests in this study has a low content of S, P or O impurities (Table 1). The powder particles show few satellites, no internal porosity, a spherical particle shape (Figures 2(a) and 2(b)), and a PSD in the typical LPBF size range (Figure 1). Therefore, the powder exhibits high flowability, high bulk, and high tap density and is suitable for processing via LPBF (Table 3). The sieved powder's lower theoretical packing density can explain the slight
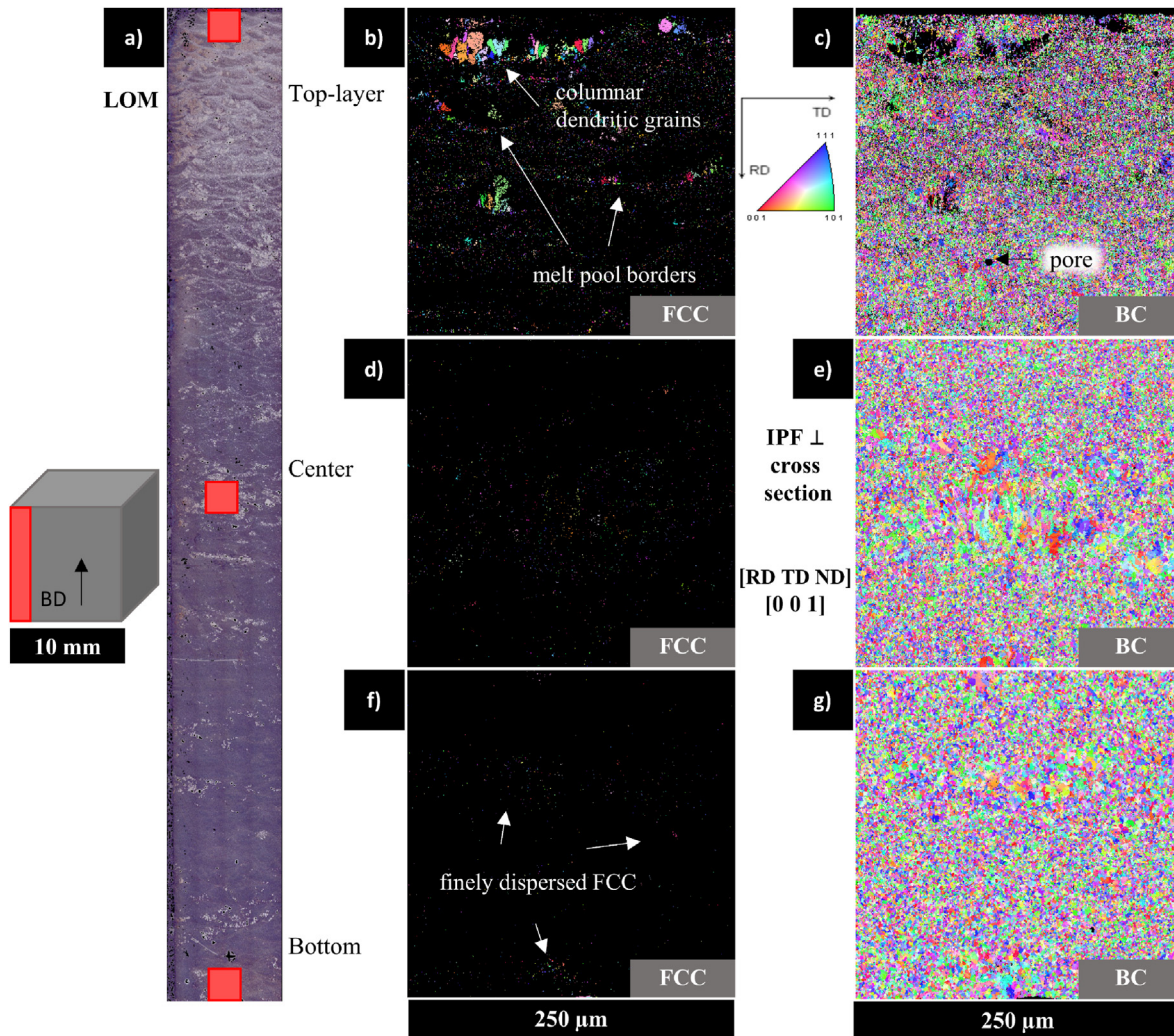
Figure 3. Light optical microscopy (LOM) image and crystal orientation maps of an as-built specimen derived via EBSD in inverse pole figure (IPF) coloring. (a) LOM image of etched cross section over the entire specimen height (red rectangle in leftmost sketched cubic specimen). (b) EBSD image of the FCC phase fraction of the top area [upper red square in 3(a)] of the specimen. (c) EBSD image of a BC phase fraction of the top area [upper red square in 3(a)] of the specimen. (d) EBSD image of the FCC phase fraction of the center area [middle red square in 3 a)]. (e) EBSD image of the BC phase fraction of the center area [middle red square in 3(a)] of the specimen. (f) EBSD image of the FCC phase fraction of the bottom area [lower red square in 3(a)]. (g) EBSD image of the BC phase fraction of the bottom area [lower red square in 3(a)] of the specimen.

decrease in tap and bulk density to a PSD typical for LPBF [32]. The significant increase in flowability can be explained by the changed storage conditions (vacuum drying) [33]. A preliminary study was carried out with this pre-processed powder. In the preliminary study, the process parameters and substrate plate temperature (500 °C, 600 °C, and 800 °C) were varied over a wide range, and only a substrate plate temperature of 800 °C enabled process-safe production of dense (>99.8%) and crack-free specimens (Table 2). HSS, with a high carbon content, tends to crack because of thermal stresses, embrittlement due to martensite formation, incoherent primary carbides, and the associated increase in stress concentration [24, 34, 35, 36]. This is especially true for the S390, which has a carbon content of 1.64 wt% and a high carbide-forming alloying element content.

In situ heat treatment (HT) of S390, which involves substrate plate heating at 800 °C during LPBF, has the following effects:

i. Increased diffusion, increased dislocation mobility, and reduced thermal gradient lower thermally induced stresses.
ii. There is a decrease in segregations due to the increased solubility of alloying elements in the austenitic FCC phase present at this temperature during LPBF [2].

iii. The solid-phase transformation from austenite to martensite during fabrication is suppressed by building up the specimens above the martensite starting temperature M_s.

Consequently, it has been possible for the first time to process S390 via LPBF without cracking, which was previously only possible via EBM [26]. A density of >99.8% was achieved using LPBF, which is significantly higher than the maximum density of 97.7% achieved with EBM. However, that in the tests with EBM in [26], a powder with high internal porosity, heteromorphic particles, and a high number of satellites was used, and according to several other studies [32, 37], these factors have a negative effect on the achievable component density.

4.1. In situ heat treatment and microstructural evolution

The HT of HSS, and specifically S390, is dependent on temperature and duration [27]. Because of the in situ HT via substrate plate heating at 800 °C during the LPBF process, layers at different heights of the specimen were heat-treated for different durations. This results in differences in the material with respect to phase transformations and the precipitation of carbides, which are reflected in specific mechanical properties [1,
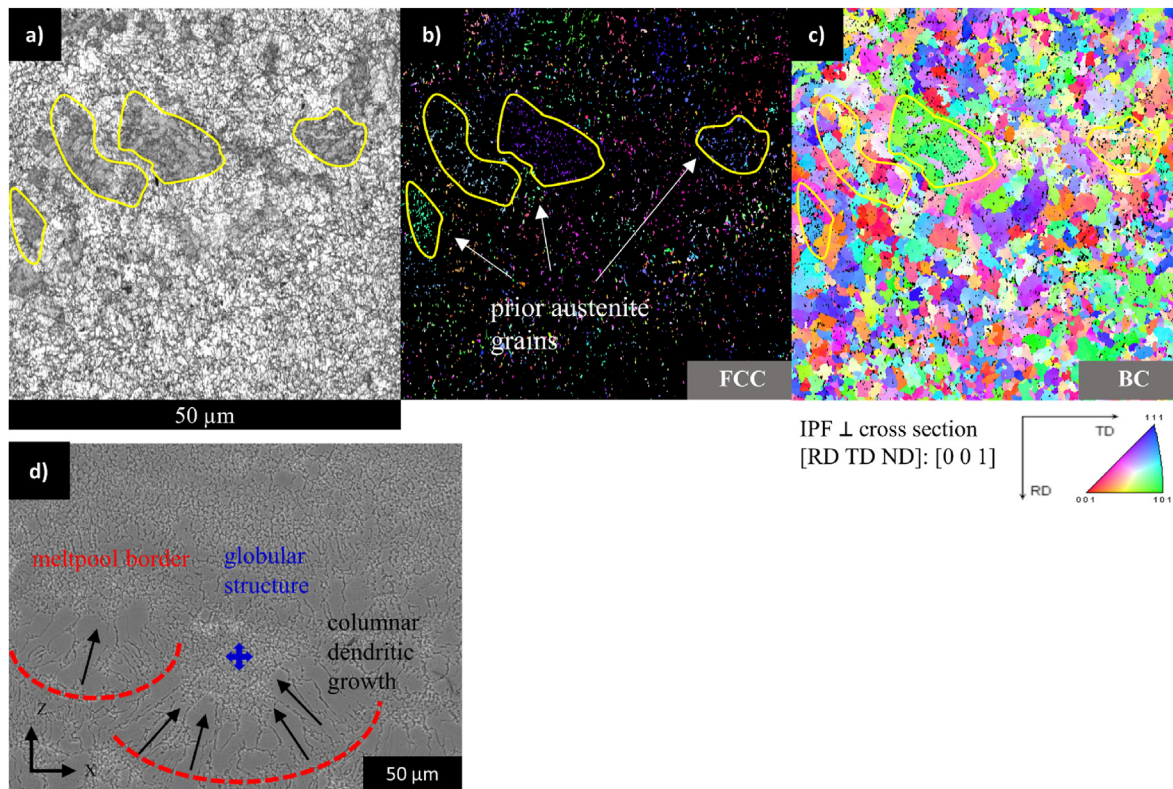
Figure 4. SEM micrographs of the center of the as-built specimen. (a) IQ (image quality) image with darker areas marked in yellow in a brighter matrix. (b) IPF mapping of the FCC phase fraction with yellow markings from 4(a). (c) IPF mapping of the BC phase fraction with yellow markings from 4(a). (d) shows a micrograph of the center area of the etched as-build specimen as an overlay of the BSE and secondary electron (SE) detectors. The Z-direction indicates the build direction. The red dashed lines indicate melt pool borders. Fine globular structures are marked in blue and columnar structures with black arrows.
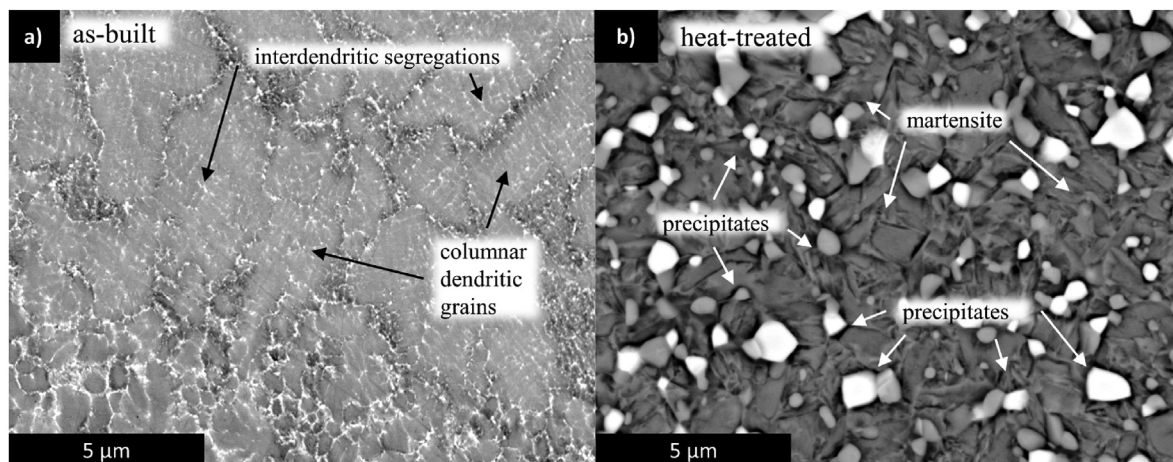

Figure 5. SEM BSE image of the center of the specimen. (a) Image of a region of an as-built specimen in which large grains with columnar dendritic growth are visible. Carbides are visible as segregations in the interdendritic areas. (b) Heat-treated specimen: precipitated carbides embedded in martensite matrix.

2, 38, 39]. For 10 mm high cube specimens produced in these experiments, the lowest layer was exposed to the 800 °C substrate plate heating for 3 h. The higher the layer in the specimen, the shorter the duration of exposure to in situ HT via substrate plate heating. In addition to the in situ HT at 800 °C via substrate plate heating, each solidified melt track underwent a brief, repeated annealing from heat exposure to adjacent and overlying melt tracks. Consequently, the top layer differs from the other layers because, first, it was annealed exclusively by laterally adjacent melt tracks and not by the fabrication of overlying layers. Second, it was exposed to in situ HT via substrate plate heating at 800 °C for a relatively short time. All layers in the as-built specimens were subjected to different durations of in situ HT via substrate plate heating. In addition, the top layer has a unique position because it is the only layer that is not reheated (i.e., annealed) to high temperatures. The resulting differences along the buildup direction are shown in the LOM image in Figure 3(a) using an etched specimen area. The in situ HT duration is shortest for the top layer, which appears bright in the LOM image, while the underlying heat-treated layers all the way down to the bottom layer appear progressively darker. This is because the nital etching of the different phases (e.g., RA, martensite, and carbides) is rendered with a different level of brightness in LOM [40]. The hardness of the specimens decreases with increasing distance from the top layer—and thus with
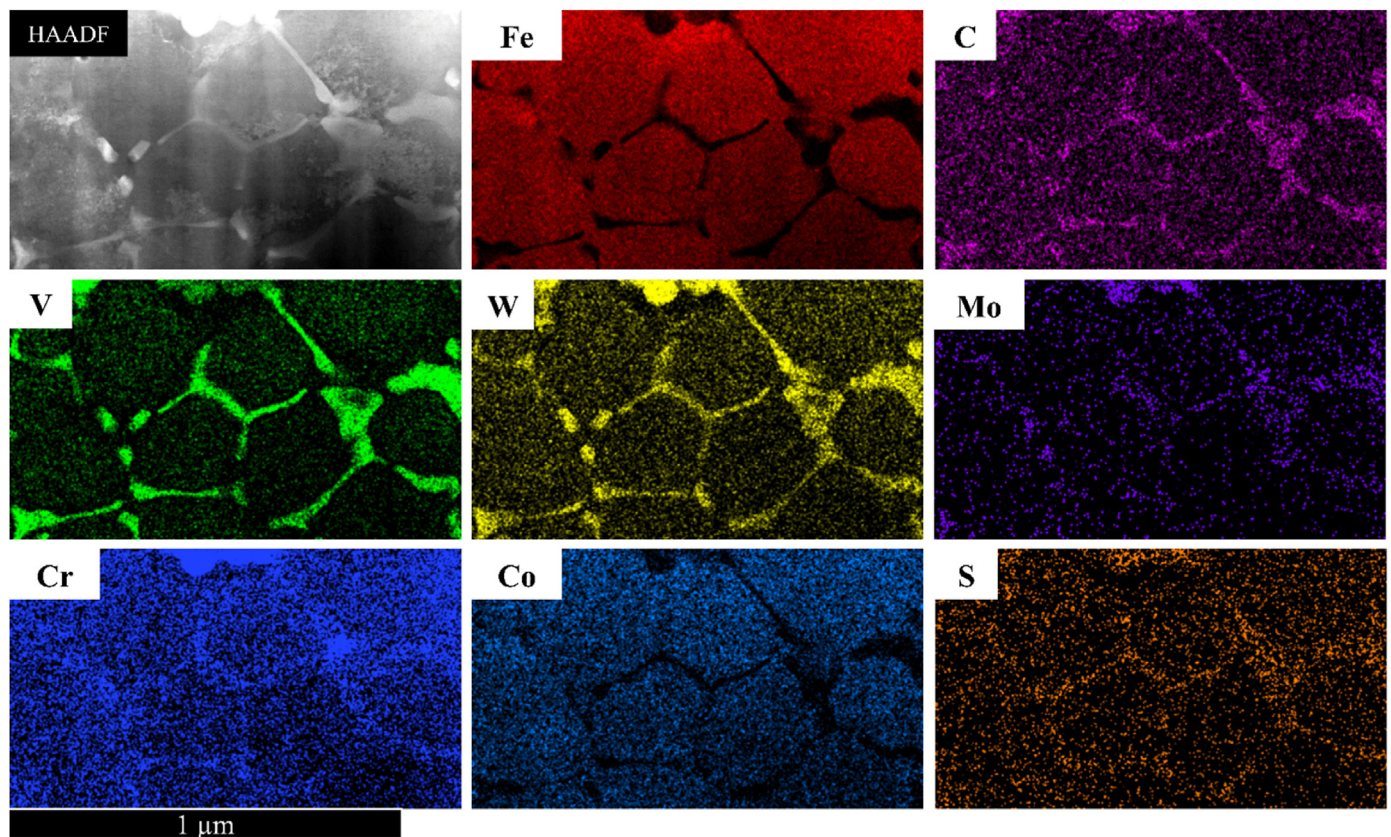
Figure 6. TEM high-angle annular dark-field (HAADF) micrographs of the columnar dendritic region of the center of the as-built specimens, including element mapping for Fe, C, V, W, Mo, Cr, Co, and S.
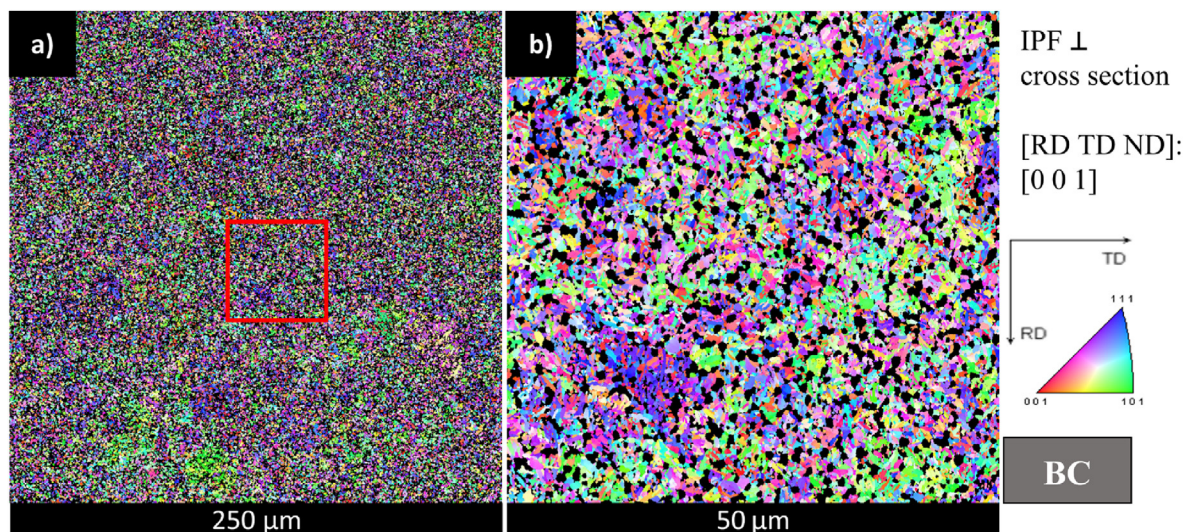

Figure 7. EBSD micrographs with BC phase fraction of the center of the heat-treated specimen: (a) lower magnification (b) higher magnification.

increasing in situ HT duration—from 798 HV1 to 499 HV1 (Figure 12). In the EBSD images, distinct columnar dendritic FCC grains are visible in the top layer (Figure 3(b)) and embedded in a fine-grained BC structure (Figure 3(c)). The XRD results for the as-built top layer indicate FCC austenite, FCC carbides, and BCT martensite (Figure 10). The FCC fraction in Figure 3(b) consists of austenitic columnar dendritic grains, which can identified as RA, and of much smaller FCC carbides. In contrast, the majority of the microstructure in the top layer BCT corresponds to martensite.

The more extended in situ heat-treated areas in the center and bottom layer of an as-built specimen appear dark in the LOM image in Figure 3(a). In the EBSD images of these areas, almost only BC phases are detected, both in the center of the specimen (Figure 3(e)) and in the bottom layer (Figure 3(g)). Examining the XRD patterns of the bottom layer presented in Figure 10, clear martensitic double peaks are visible. Therefore, the BC phases in the bottom layer can be identified as martensitic BCT phases [41].
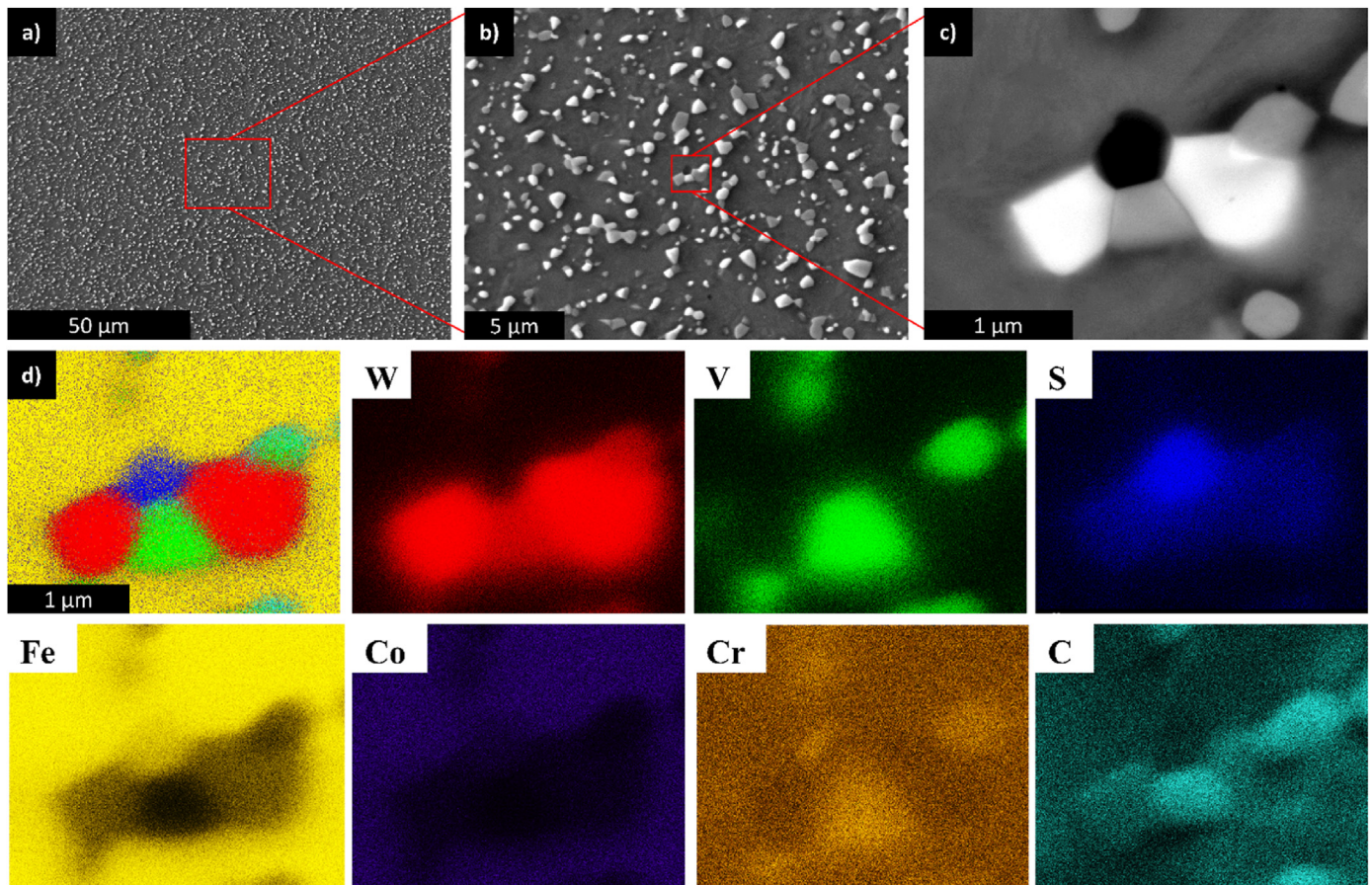
Figure 8. SEM BSE micrographs and EDX mappings of heat-treated specimens. (a) an overview showing homogeneously distributed precipitated carbides. (b) distinguishable carbides: white-colored grains are tungsten-rich carbides, and gray-colored phases are vanadium-rich carbides. (c) detailed view showing a carbide cluster embedded in the Fe matrix. (d) merged EDX element mapping of a carbide cluster, followed by a mapping for each element.

In the EBSD image of the as-built specimens in the center and in the bottom layer (Figures 3(d) and 3(f)), at the given magnification of the 250 µm square, the FCC fraction is visible as finely distributed phases in each case. Coarse residual austenite grains as in the top layer are not found in these two areas. This is confirmed by the XRD results, which show no austenite peak for the bottom layer (Figure 10). At the higher magnification in the 50 µm square in Figure 4(b) at the center area of the as-built specimen the detected FCC phases have sizes in the sub-micrometer range, are finely distributed, and are arranged in equally oriented clusters. The dimensions and spacing of these FCC phases, as well as their location in the grain interior, match the interdendritic segregations observed in the SEM BSE image in Figure 5(a). In the TEM image in Figure 6, interdendritic segregations from the specimen center of the as-built specimens are shown in high resolution and show enrichments of C in combination with the carbide-forming elements V, W, Mo, and Cr in the element mapping. This composition has been reported in the literature for the primary FCC MC carbides [23, 26, 39]. The elongated shape and cellular arrangement in Figure 6 indicate that the carbides are segregated in the interdendritic spaces during solidification. The FCC MC carbides can also be detected in the bottom layer in situ heat-treated via XRD (Figure 10). Furthermore, a publication by Jin et al. [26] reports that interdendritic MC primary carbides with similar sizes and spacing are observed during EBM processing of S390.

Based on the identified and localized phases, the microstructural evolution of built-up specimens can now be traced. In the top layer, columnar dendritic RA grains are located at the edges of former LPBF melt pools (Figure 3(b)). The grain growth of the columnar dendritic grains occurs along the temperature gradient in the melt pool, progressing radially from the melt pool edge inward to the melt pool center,

as shown in Figure 4 (d). During the grain formation process, alloying elements dissolved in the melt are rejected at the solidification front (i.e., at the austenitic dendrite), and these segregate at the interdendritic interstices, as shown in Figure 6, or at the grain boundaries. Fischmeister et al. report that MC carbides can form both eutectically and as primary grains from the melt [42]. In the melt pool center, columnar dendritic grains are no longer observed due to a locally reduced temperature gradient, causing a transition to equiaxed solidification [26, 27]. Once solidified, dendritic regions can be partially remelted by adjacent or subsequent melt traces or heat treated at temperatures close to liquidus. This results in structures similar to those shown in Figure 4(d) and Figure 5(a), consisting of columnar dendritic grains, equiaxed grains, and segregations at the grain boundaries and interdendritic interstices. Similar equiaxial and columnar dendritic structures have been reported for EBM of S390, but the structures are much larger than in LBPF [26]. A differentiation between small equiaxial grains with high angle grain boundaries, dendrite arms and solidification cells with small angle grain boundaries will be the task of further investigations and will be presented in another publication.

The top layer is only minimally in situ heat-treated via substrate plate heating and only minimally annealed by adjacent areas, and it has a similar microstructure as S390 powder particles. In the S390 powder, the metallic matrix phase is mainly present as RA. This is evidenced by the XRD phase analysis of the powder, which identifies austenite and MC in Figure 10 and matches the dendritic structures and interdendritic segregations of the powder particles in the SEM images (Figure 2(a) and Figure 2(d)).

In essence, after solidification of the meltpool and cooling to 800 °C, FCC phase austenite is present in columnar and equiaxed grains
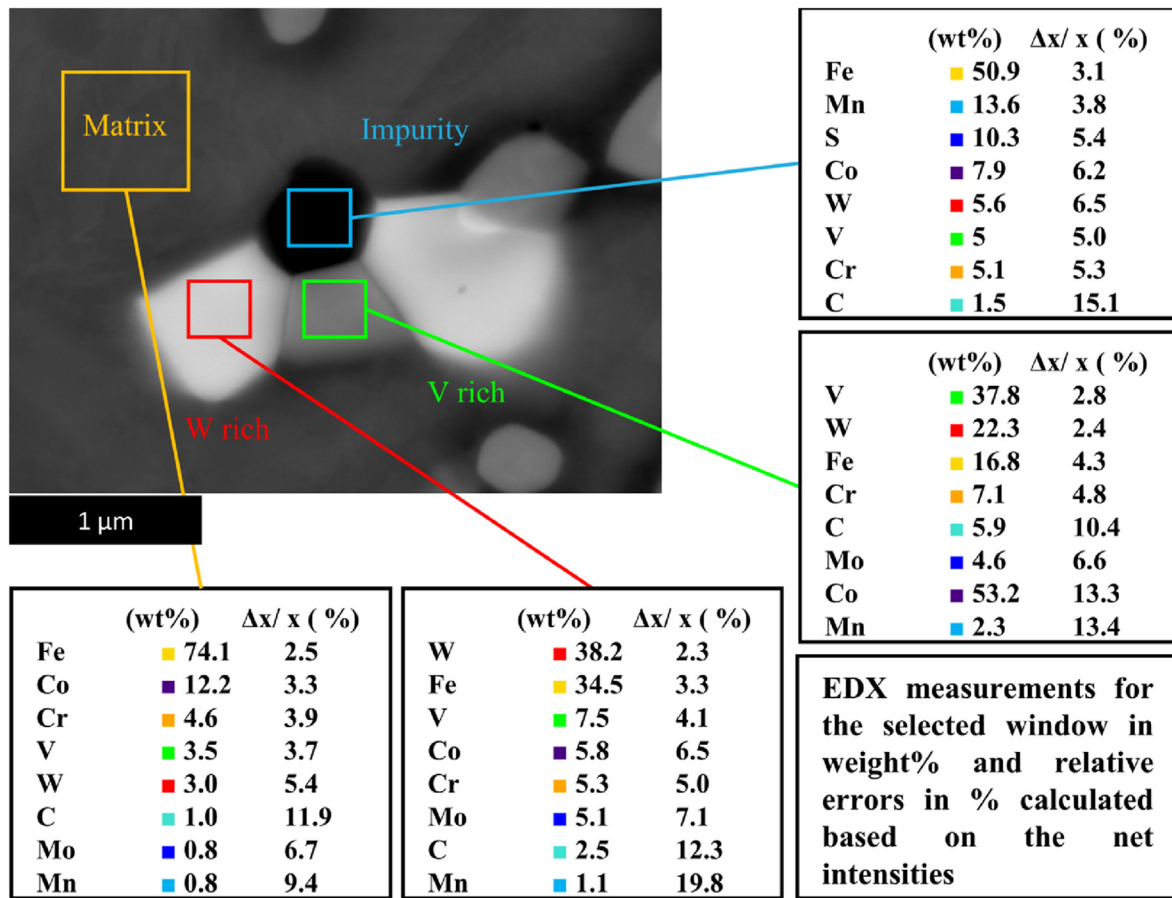
Figure 9. SEM BSE micrograph of the area of the heat-treated specimen of Figure 8, including an EDX mapping of the sections. Four areas are classified: the matrix comprising mainly Fe, Co, and Cr, and having a high C content; a W and Fe rich grain mixed with some V, Co, Cr, and Mo; a vanadium-rich particle with high contents of Cr and Mo; impurity rich in S and Mn.
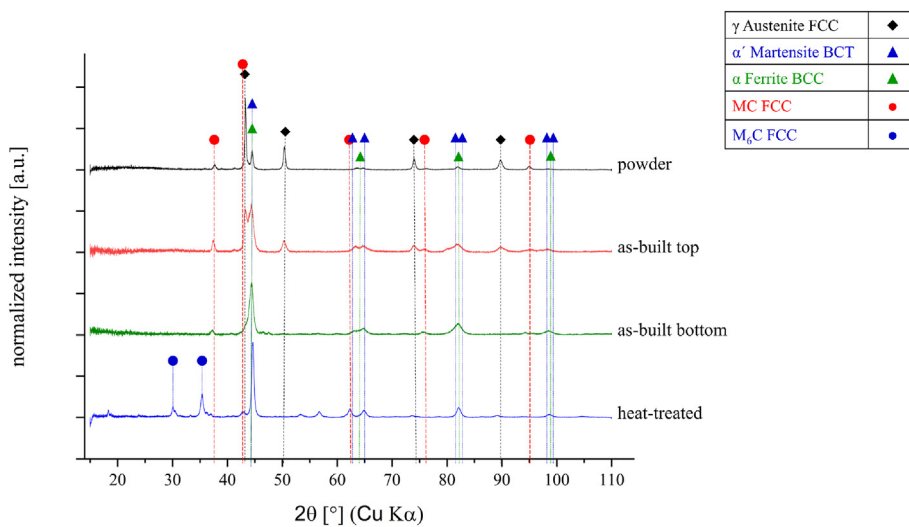

Figure 10. Phase identification via comparison of the XRD patterns of the powder, as-built top and tempered layers, and the heat-treated specimens across the Fe phases: austenite γ-Fe FCC, α' martensite BCT (double peaks), α-Fe ferrite BCC, and the peaks of the carbides MC FCC and M_6C FCC. For the powder, there are peaks for austenite and MC, and weak peaks of martensite or ferrite are visible. In the as-built top layer, distinct peaks for austenite, martensite, and MC are visible. For the as-built bottom layer, martensite and MC are identifiable. The heat-treated specimen shows peaks for martensite, MC, and M_6C.

accompanied by primary carbides. Martensite formation from austenite occurs only during the eventual cooling from 800 °C and the temperature falling below M_s. As mentioned earlier, the duration of in situ HT at 800 °C increases from the top to the bottom layers. The in situ HT of the rapid solidified austenite at 800 °C leads to the reduction of internal stresses and a high dislocation density on the one hand, and on the other hand, to the precipitation of the carbon C and other alloying elements in the form of carbides at the grain or dendrite boundaries [26]. Thus, with increasing in situ HT duration, the carbon content in the austenite decreases toward the bottom layer. The local composition of the austenite grains determines their M_s [43, 44]. Thus, the annealing of austenite, in situ HT at 800 °C, and the resulting precipitation of alloying elements increases the M_s and promotes the transformation of austenite to martensite [44, 45, 46]. Ultimately, upon cooling, this forms a softer, less
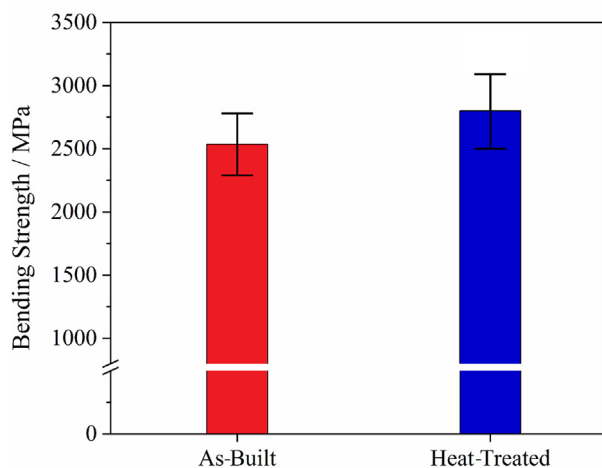
Figure 11. Bending strength of the as-built and heat-treated specimens.
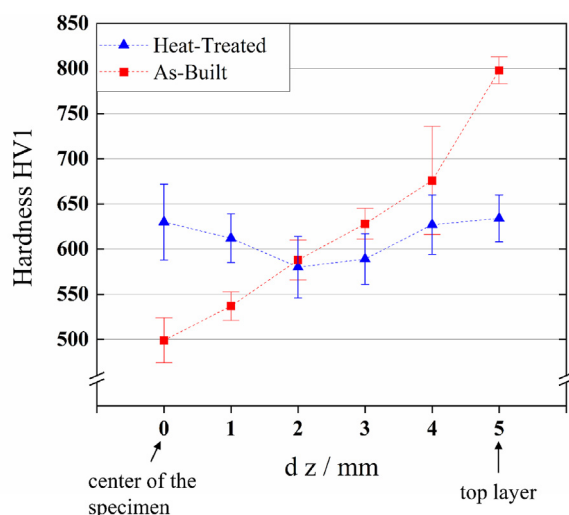

Figure 12. HV1 measurements show the hardness gradient along the buildup direction for as-built and heat-treated specimens, starting at the center of the specimen in 1 mm iterations until the top layer at 5 mm.

tetragonally distorted martensite with a hardness gradient corresponding to the in situ HT duration [23, 47], similar to the *autotempered* martensite as reported by Jin et al. [26]. Thus, large dendritic structures indicate prior austenite grains (Figures 4(a) and 4(b)), which can be identified after cooling as a fine-grained martensitic microstructure in EBSD images (Figure 4(c)) and XRD patterns (Figure 10).

4.2. Heat treatment

The conventional HT of HSS, performed as a separate subsequent process, serves to dissolve the alloying elements during austenitizing, obtaining a supersaturated martensitic matrix via quenching. Then, during triple tempering, HT relaxes the martensite, transforming the RA, and finely precipitating the secondary carbides [1, 2, 48]. In Figure 5, the SEM BSE images show a comparison of the as-built and heat-treated specimens. The interdendritic segregations visible in the as-built specimen in Figure 5(a) are no longer visible after HT (Figure 5(b)). Similarly, the dendritic columnar and equiaxed grains of the matrix are no longer visible after HT. Figure 5(b) shows a fine-grained martensitic structure and equiaxial precipitates, which is a similar microstructure to that reported by Peng et al. [23] for heat-treated PM S390. In the XRD in Figure 10, it is clear that in the HT state, there is a preponderance of

martensite, and no RA peaks are visible. In the EBSD images in Figure 7, fine BC phases of a few μm in size can be seen, matching the description of martensite in the literature [23]. The BC matrix is homogeneously interspersed with precipitates, as shown in Figure 7 and Figure 8. These precipitates differ in brightness in the BSE images (Figures 5(b) and 8(c)). In the EDX element mapping in Figure 8 and in the breakdown of the mass fractions of the alloying elements in Figure 9, different types of precipitates can be distinguished:

i. One type, which appears bright in the BSE, is rich in W and Fe and has a high C content in the element mapping. The EDX mapping of this particle in Figure 9 shows the mass fractions with approximately equal amounts of Fe (35 wt%) and W (38 wt%), and a high C content. In the XRD patterns, it can be identified by its characteristic peaks as M_6C—more precisely, as Fe_3W_3C. However, it should be mentioned that atomic percentages do not correspond to the stoichiometry of the phase with 14.3 at% W and 42.5 at% Fe.

ii. The gray phase in the BSE image has a high V content (38 wt%) in the element mapping (Figure 9), accompanied by high proportions of C, W, Cr, and Mo. The vanadium-rich particle is probably an MC vanadium carbide (VC) mixed with MC in various proportions. The MC peak is superimposed on the martensite peak in the XRD spectra (Figure 10), making it difficult to distinguish one from the other [26].

iii. The black phase in the BSE image is an impurity rich in Mn (13.6 wt%) and S (10.3 wt%). Such impurities occur only occasionally.

It has been reported in the literature that the carbides in heat-treated S390 specimens are primarily Fe_3W_3C and VC, comparable in size and distribution to those observed in this study [3, 4, 22, 23, 39].

Subsequent HT compensates for differences in the as-built specimens and transforms the primary microstructure into a homogenized, fine-grained martensitic matrix with precipitated secondary carbides (Figure 5 and Figure 7).

4.3. Mechanical properties compared to state-of-the-art

The as-built specimens have a bending strength of 2535 MPa, taking into account that the area of the bending specimen with tensile load was in situ heat treated for a longer duration, and the area with compressive load only for a short time. The hardness values of the as-built specimens range from 798 HV1 in the top layer to 499 HV1 in the longer in situ heat-treated layers toward the bottom (Figure 12). Because the carbide precipitates do not change significantly across the specimen height, the hardness gradient across height is primarily due to differences in martensite hardness. Subsequent HT can increase bending strength to about 2800 MPa, with an average hardness of 611 HV1 (Table 4). According to the manufacturer, a hardness of 63 HRC can be achieved with this HT via HIP, but these values could not be achieved with the LPBF specimens treated with a furnace without inert atmosphere [1] HT homogenizes the microstructure and hardness of the specimen and causes the dissolution of alloying elements, the reformation of fine martensite grains, and the precipitation of secondary carbides at small intervals (micrometer to submicrometer in size) at all positions in the specimen.

Table 4. Mechanical properties (bending strength and hardness) of the as-built and heat-treated specimens.

	Mean Bending Strength (MPa)	Max (MPa)	Min (MPa)	Mean Hardness (HV1)	Max. Hardness (HV1)	Min. Hardness (HV1)
As-Built	2,535	2,775	2,330	_ _	798	499
Heat-Treated	2,799	3,504	2,613	611	663	561

The solid solution strengthening is caused primarily by the alloying elements Co (12 wt%), Cr (5 wt%), and C (1 wt%) dissolved in the martensitic matrix (Figure 9). Temperature-resistant primary carbides, which are not dissolved during HT (e.g., Mo carbides), hinder the grain growth of the austenite grains during solution annealing [39]. Figure 7 shows fine martensite grains contributing to grain boundary strengthening via the Hall–Petch mechanism [27]. In Figure 7, and in the SEM BSE images (Figure 8(a)), uniform fine precipitated carbide grains approximately 1 μm size are visible; these cause precipitation hardening via the Orowan mechanism [27, 28].

The mechanical properties of the specimens can be further improved by HT under HIP conditions, as has already been demonstrated for EBM specimens in the Jin et al. study [26]. Such a treatment is also standard for PM S390. However, because LPBF specimens have not yet been subjected to HT under HIP conditions, a comparison with conventionally produced PM S390 is not yet possible.

5. Conclusions

This is the first study to investigate the processing of PM HSS S390 via LPBF, and it provides a detailed analysis of dense and crack-free as-built specimens, as well as heat-treated specimens. The conclusions of the study are as follows:

- HSS S390 can be processed via LPBF crack-free, with a relative density of 99.8% achieved through in situ HT at up to 800 °C.
- As-built specimens exhibit changing microstructure and phases depending on temperature history and specimen height, with distinguishable columnar dendritic and equiaxed grains. Segregated intergranular carbides (several microns) and interdendritic carbides (submicron) are visible. Interdendritic MC carbides are identifiable and contain V, W, Cr, and C.
- Heat-treated specimens show homogenous microstructure and evenly distributed micron- and submicron-sized secondary carbides. Due to HT, MC (predominantly VC) and M_6C (predominantly Fe_3W_3C) are precipitated.
- The achieved mechanical properties are as follows:
  o As-built: a mean bending strength of 2535 ± 148 MPa, and a hardness gradient along the specimen height of 500 HV1 to 800 HV1.
  o Heat treated: a mean bending strength of 2799 ± 278 MPa, with a mean hardness value of 610 ± 50 HV1.

LPBF in situ HT is sufficient to suppress crack mitigation in HSS S390. Subsequent conventional HT improves mechanical properties and homogenizes the microstructure of as-built specimens, which are similar to PM [1] and EBM [26] specimens. The results indicate an evident influence of thermal history on the microstructure and resulting mechanical properties of the manufactured specimens In-situ-HT in the LPBF build chamber, but post-process might overcome the gradients of hardness and microstructure along the building direction of the as-built specimens. Future research may experiment with alternative heating concepts for comparison against the substrate plate heating approach investigated in this study (e.g., radiation-based heating for the top layer of the specimen using infrared heating modules or large area diodes) and evaluate the effect on the resulting microstructure [49, 50, 51, 52].

Declarations

Author contribution statement

Simon Bergmüller: Conceived and designed the experiments; Performed the experiments; Analyzed and interpreted the data; Contributed reagents, materials, analysis tools or data; Wrote the paper.

Lukas Kaserer: Conceived and designed the experiments; Analyzed and interpreted the data.

Lorenz Fuchs: Performed the experiments.

Jakob Braun: Analyzed and interpreted the data.

Nikolaus Weinberger: Contributed reagents, materials, analysis tools or data.

Ilse Letofsky-Papst: Analyzed and interpreted the data; Contributed reagents, materials, analysis tools or data.

Gerhard Leichtfried: Analyzed and interpreted the data; Wrote the paper.

Data availability statement

Data will be made available on request.

Declaration of interests statement

The authors declare no conflict of interest.

Additional information

No additional information is available for this paper.

References

[1] Voestalpine Böhler Edelstahl GmbH & Co KG, Böhler S390 High Speed Steel - Technical Brochure. https://www.bohler-edelstahl.com/media/S390DE.pdf, 2010.
[2] H. Peng, L. Hu, L. Li, L. Zhang, X. Zhang, Evolution of the microstructure and mechanical properties of powder metallurgical high-speed steel S390 after heat treatment, J. Alloys Compd. 740 (2018) 766–773.
[3] E.P. Nikolaeva, D.B. Vlasov, Effect of heat treatment conditions on structure and properties of high-speed steel, IOP Conf. Ser. Mater. Sci. Eng. (2017).
[4] M. Godec, B.Š. Batič, D. Mandrino, A. Nagode, V. Leskovšek, S.D. Škapin, M. Jenko, Characterization of the carbides and the martensite phase in powder-metallurgy high-speed steel, Mater. Char. 61 (2010) 452–458.
[5] Boehler, Böhler S390 Microclean Datasheet. https://www.bohler-edelstahl.com/app/uploads/sites/92/2022/04/productdb/api/s390-microclean_de.pdf, 2022.
[6] J. Van Humbeeck, S. Buls, L. Thijs, K. Kempen, B. Vrancken, J.-P. Kruth, Selective laser melting of crack-free high density M2 high speed steel parts by baseplate preheating, J. Manuf. Sci. Eng. 136 (2014), 061026.
[7] Z. Liu, C. Chua, K. Leong, K. Kempen, L. Thijs, E. Yasa, J. Van-Humbeeck, J. Kruth, A preliminary investigation on Selective Laser Melting of M2 high speed steel, Innov. Dev. Virtual Phys. Prototyp. (2011) 339–346.
[8] L. Zumofen, C. Beck, A. Kirchheim, H.-J. Dennig, Quality related effects of the preheating temperature on laser melted high carbon content steels, in: Ind. Addit. Manuf. - Proc. Addit. Manuf. Prod. Appl. - AMPA2017, Springer International Publishing, 2018, pp. 210–219.
[9] J. Kunz, J. Saewe, S. Herzog, A. Kaletsch, J.H. Schleifenbaum, C. Broeckmann, Title: Mechanical Properties of High Speed Steel AISI M50 Produced by Laser Powder Bed Fusion, 2019.
[10] J. Krell, A. Röttger, K. Geenen, W. Theisen, General investigations on processing tool steel X40CrMoV5-1 with selective laser melting, J. Mater. Process. Technol. 255 (2018) 679–688.
[11] J. Boes, A. Röttger, C. Mutke, C. Escher, W. Theisen, Microstructure and mechanical properties of X65MoCrWV3-2 cold-work tool steel produced by selective laser melting, Addit. Manuf. 23 (2018) 170–180.
[12] R. Mertens, B. Vrancken, N. Holmstock, Y. Kinds, J.P. Kruth, J. Van Humbeeck, Influence of powder bed preheating on microstructure and mechanical properties of H13 tool steel SLM parts, in: Phys. Procedia, Elsevier B.V., 2016, pp. 882–890.
[13] R. Casati, M. Coduri, N. Lecis, C. Andrianopoli, M. Vedani, Microstructure and mechanical behavior of hot-work tool steels processed by Selective Laser Melting, Mater. Char. 137 (2018) 50–57.
[14] S. Bremen, W. Meiners, A. Diatlov, Selective laser melting, Laser Technol. J. 9 (2012) 33–38.
[15] Y. He, M. Zhong, J. Beuth, B. Webler, A study of microstructure and cracking behavior of H13 tool steel produced by laser powder bed fusion using single-tracks, multi-track pads, and 3D cubes, J. Mater. Process. Technol. 286 (2020), 116802.

[16] F. Feuerhahn, A. Schulz, T. Seefeld, F. Vollertsen, Microstructure and properties of selective laser melted high hardness tool steel, in: Phys. Procedia, Elsevier B.V., 2013, pp. 843–848.

[17] K. Geenen, A. Röttger, F. Feld, W. Theisen, Microstructure, mechanical, and tribological properties of M3:2 high-speed steel processed by selective laser melting, hot-isostatic pressing, and casting, Addit. Manuf. 28 (2019) 585–599.

[18] J. Saewe, M.B. Wilms, Influence of Preheating Temperature on Hardness and Microstructure of High-Speed Steel Hs6-5-3-8, 2019.

[19] J. Saewe, N. Carstensen, P. Kürnsteiner, E.A. Jägle, J.H. Schleifenbaum, Influence of increased carbon content on the processability of high-speed steel HS6-5-3-8 by laser powder bed fusion, Addit. Manuf. 46 (2021) 102125.

[20] F. Galbusera, A.G. Demir, J. Platl, C. Turk, R. Schnitzer, B. Previtali, Processability and cracking behaviour of novel high-alloyed tool steels processed by Laser Powder Bed Fusion, J. Mater. Process. Technol. 302 (2022), 117435.

[21] V. Leskovšek, B. Podgornik, Vacuum heat treatment, deep cryogenic treatment and simultaneous pulse plasma nitriding and tempering of P/M S390MC steel, Mater. Sci. Eng. 531 (2012) 119–129.

[22] H. Peng, L. Hu, L. Li, L. Zhang, X. Zhang, Evolution of the microstructure and mechanical properties of powder metallurgical high-speed steel S390 after heat treatment, J. Alloys Compd. 740 (2018) 766–773.

[23] H. Peng, L. Hu, X. Zhang, X. Wei, L. Li, J. Zhou, Microstructural evolution, behavior of precipitates, and mechanical properties of powder metallurgical high-speed steel S390 during tempering, Metall. Mater. Trans. A Phys. Metall. Mater. Sci. 50 (2019) 874–883.

[24] Y. Torres, S. Rodr, A. Mateo, M. Anglada, L. Llanes, Fatigue Behavior of Powder Metallurgy High-Speed Steels : Fatigue Limit Prediction Using a Crack Growth Threshold-Based Approach, Mater. Sci. Eng. A 389 (2004) 501–504.

[25] M. Niederkofler, M. Leisch, 3D-atom probe characterization of nano-precipitates in a PM processed tool steels, in: Appl. Surf. Sci., Elsevier, 2004, pp. 132–138.

[26] J. Jin, R. Gao, H. Peng, H. Guo, S. Gong, B. Chen, Rapid solidification microstructure and carbide precipitation behavior in electron beam melted high-speed steel, Metall. Mater. Trans. A Phys. Metall. Mater. Sci. 51 (2020) 2411–2429.

[27] B. Ilschner, R. Singer, Werkstoffwissenschaften und Fertigungstechnik, 2005. https://link.springer.com/content/pdf/10.1007/978-3-642-53891-9.pdf. (Accessed 4 March 2022).

[28] A.J. Ardell, Precipitation hardening, Metall. Trans. A 16 (1985) 2131–2165.

[29] L. Kaserer, J. Braun, J. Stajkovic, K.H. Leitz, B. Tabernig, P. Singer, I. Letofsky-Papst, H. Kestler, G. Leichtfried, Fully dense and crack free molybdenum manufactured by Selective Laser Melting through alloying with carbon, Int. J. Refract. Met. Hard Mater. 84 (2019), 105000.

[30] P. Bajaj, A. Hariharan, A. Kini, P. Kürnsteiner, D. Raabe, E.A. Jägle, Steels in additive manufacturing: a review of their microstructure and properties, Mater. Sci. Eng. 772 (2020), 138633.

[31] Y.M. Wang, T. Voisin, J.T. McKeown, J. Ye, N.P. Calta, Z. Li, Z. Zeng, Y. Zhang, W. Chen, T.T. Roehling, R.T. Ott, M.K. Santala, P.J. Depond, M.J. Matthews, A.V. Hamza, T. Zhu, Additively manufactured hierarchical stainless steels with high strength and ductility, Nat. Mater. 17 (2018) 63–70.

[32] K. Riener, N. Albrecht, S. Ziegelmeier, R. Ramakrishnan, L. Haferkamp, A.B. Spierings, G.J. Leichtfried, Influence of particle size distribution and morphology on the properties of the powder feedstock as well as of AlSi10Mg parts produced by laser powder bed fusion (LPBF), Addit, Man 34 (2020), 101286.

[33] K. Riener, S. Oswald, M. Winkler, G.J. Leichtfried, Influence of storage conditions and reconditioning of AlSi10Mg powder on the quality of parts produced by laser powder bed fusion (LPBF), Addit, Man 39 (2021), 101896.

[34] J.L. Bartlett, X. Li, An overview of residual stresses in metal powder bed fusion, Addit. Manuf. 27 (2019) 131–149.

[35] P.J. Withers, H.K.D.H. Bhadeshia, Residual stress part 2 - nature and origins, Mater. Sci. Technol. 17 (2001) 366–375.

[36] F. Meurling, A. Melander, M. Tidesten, L. Westin, Influence of carbide and inclusion contents on the fatigue properties of high speed steels and tool steels, Int. J. Fatig. 23 (2001) 215–224.

[37] F. Chu, K. Zhang, H. Shen, M. Liu, W. Huang, X. Zhang, E. Liang, Z. Zhou, L. Lei, J. Hou, A. Huang, Influence of satellite and agglomeration of powder on the processability of AlSi10Mg powder in Laser Powder Bed Fusion, J. Mater. Res. Technol. 11 (2021) 2059–2073.

[38] S. Karagöz, I. Liem, E. Bischoff, H.F. Fischmeister, Determination of carbide and matrix compositions in high-speed steels by analytical electron microscopy, Metall. Trans. A 20 (1989) 2695–2701.

[39] H. Peng, L. Hu, T. Ngai, L. Li, X. Zhang, H. Xie, W. Gong, Effects of austenitizing temperature on microstructure and mechanical property of a 4-GPa-grade PM high-speed steel, Mater. Sci. Eng. 719 (2018) 21–26.

[40] G. Petzow, Metallographisches, keramographisches und plastographisches Ätzen, Schweizerbart Science Publishers, Stuttgart, Germany, 2006. http://www.sch weizerbart.de//publications/detail/isbn/9783443230166/Petzow_Metall_Kera m_u_Plastogr_Atz.

[41] T. Tanaka, N. Maruyama, N. Nakamura, A.J. Wilkinson, Tetragonality of Fe-C martensite – a pattern matching electron backscatter diffraction analysis compared to X-ray diffraction, Acta Mater. 195 (2020) 728–738.

[42] H.F. Fischmeister, R. Riedl, S. Karagöz, Solidification of high-speed tool steels, Metall. Trans. A 20 (1989) 2133–2148.

[43] J. Platl, H. Leitner, C. Turk, R. Schnitzer, Determination of martensite start temperature of high-speed steels based on thermodynamic calculations, Steel Res. Int. 91 (2020) 1–8.

[44] B. Edenhofer, D. Joritz, M. Rink, K. Voges, Carburizing of steels, in: Thermochem. Surf. Eng. Steels Improv. Mater. Perform., Woodhead Publishing, 2015, pp. 485–553.

[45] K.C. Hwang, S. Lee, H.C. Lee, Effects of alloying elements on microstructure and fracture properties of cast high speed steel rolls: Part I: microstructural analysis, Mater. Sci. Eng. 254 (1998) 282–295.

[46] H. Vetters, Transformation of austenite into bainitic ferrite and martensite, Steel Res. 67 (1996) 408–411.

[47] M. Ohring, Engineering Materials Science, accessed April 14, 2022, https://boo ks.google.com/books/about/Engineering_Materials_Science.html?hl=de&i d=LcvgiCbOo38C, 1995.

[48] Anon, Tool STEELS, Am Iron Steel Inst Steel Prod Man, 1978, pp. 157–163.

[49] Heraeus entwickelt Infrarot-Wärmetechnologie für additive Fertigung - INDUSTRIAL Production ONLINE (n.d.), https://www.industrial-production.de /additive-fertigung/waermetechnologie-fuer-additive-fertigung.htm. (Accessed 17 March 2021).

[50] Hoch hinaus mit VCSEL-Heizung - Fraunhofer ILT (n.d.), https://www.ilt.fraunh ofer.de/de/presse/pressemitteilungen/pm2018/pressemitteilung-2018-10-4.html. (Accessed 17 March 2021).

[51] J.D. Roehling, W.L. Smith, T.T. Roehling, B. Vrancken, G.M. Guss, J.T. McKeown, M.R. Hill, M.J. Matthews, Reducing residual stress by selective large-area diode surface heating during laser powder bed fusion additive manufacturing, Addit. Manuf. 28 (2019) 228–235.

[52] G. Graf, N. Nouri, S. Dietrich, F. Zanger, V. Schulze, Dual-laser pbf-lb processing of a high-performance maraging tool steel fenicomovtial, Materials 14 (2021) 4251.